

Determination of solar cycle variations of midlatitude ELF/VLF chorus and hiss via automated signal detection

D. I. Golden,¹ M. Spasojevic,¹ and U. S. Inan^{1,2}

Received 7 October 2010; revised 30 November 2010; accepted 30 December 2010; published 24 March 2011.

[1] An automated algorithm for detecting chorus and hiss emissions in ground-based extremely low frequency/very low frequency (ELF/VLF) wave receiver data is developed and applied to 10 years of data collected at Palmer Station, Antarctica ($L = 2.4$, 50°S invariant latitude). The algorithm consists of three major processing steps. First, sferics and power line hum are removed from the broadband data. Second, individual events are detected and a set of 19 scalar event parameters are determined. Finally, on the basis of the parameters, detected events are categorized by a sequential pair of neural networks as either chorus, hiss, or noise. The detector runs on a modern 8-core computer at a speed of 350x real time. Results of training indicate that the neural networks are capable of differentiating between noise and emissions with a 92% success rate and between chorus and hiss with an 84% success rate. Data collected at Palmer from May 2000 to May 2010 were processed, and yearly and seasonal trends of chorus and hiss are analyzed. Yearly occurrence rates of chorus and hiss are strongly dependent on the geomagnetic disturbance level, as measured by K_p and AE , whereas seasonal occurrence rates are more strongly dependent on variations of the day/night terminator and associated variations in ionospheric absorption.

Citation: Golden, D. I., M. Spasojevic, and U. S. Inan (2011), Determination of solar cycle variations of midlatitude ELF/VLF chorus and hiss via automated signal detection, *J. Geophys. Res.*, 116, A03225, doi:10.1029/2010JA016193.

1. Introduction

[2] Extremely low frequency/very low frequency (ELF/VLF) chorus and hiss are two common types of electromagnetic waves that are spontaneously generated in the Earth's magnetosphere. Both are thought to play major roles in the acceleration [e.g., Meredith *et al.*, 2002; Horne *et al.*, 2003, 2005] and loss [e.g., Lyons *et al.*, 1972; Lyons and Thorne, 1973; Abel and Thorne, 1998] of energetic electrons in the Earth's radiation belts.

[3] The main distinguishing feature between chorus and hiss is in their frequency-time structure. Chorus is characterized by a closely spaced series of discrete tones, usually rising in frequency with time, at a rate of up to a few kHz/s [e.g., Storey, 1953]. Hiss, however, is an incoherent emission which exhibits no obvious structure [e.g., Helliwell, 1965, p. 207]. In this paper, we define chorus and hiss based on these spectral characteristics, assuming that the signal-to-noise ratio of the data is sufficient to distinguish them.

[4] Various types of hiss permeate the magnetosphere (see section 1 of Golden *et al.* [2009] for a short review), including

auroral hiss [e.g., Jørgensen, 1968; Makita, 1979], plasmaspheric hiss [e.g., Thorne *et al.*, 1973; Parady *et al.*, 1975; Meredith *et al.*, 2004], exohiss (plasmaspheric hiss which has escaped from the plasmasphere) [e.g., Thorne *et al.*, 1973] midlatitude hiss [e.g., Taylor and Gurnett, 1968; Dunckel and Helliwell, 1969], and ELF hiss [e.g., Russell *et al.*, 1972]. These terms are particularly confusing because many permutations of them may be observed within the plasmasphere, at midlatitudes, and in the ELF range, besides the obvious eponymous varieties. Of these, only plasmaspheric hiss and exohiss are thought to occur below ~ 2 kHz at midlatitudes, and although the prevailing belief is that plasmaspheric hiss cannot penetrate to the ground due to its magnetospheric reflection near the local lower hybrid resonance frequency [Thorne and Kennel, 1967], ground observations by Golden *et al.* [2009] at Palmer Station, Antarctica, suggest that a subset of plasmaspheric hiss may in fact reach the ground at midlatitudes. Therefore observations of hiss on the ground at midlatitudes such as those presented in this paper may include both plasmaspheric hiss and exohiss.

[5] Chorus and hiss emissions, regardless of their magnetospheric source, are frequently observed at midlatitude and high-latitude ground stations [e.g., Laaspere *et al.*, 1964; Golden *et al.*, 2009; Smith *et al.*, 2010]. Although the large number of observed emissions presents a boon for scientific statistics, it has traditionally been difficult to categorize emissions on a large scale. Past attempts have typically used

¹Electrical Engineering Department, Stanford University, Stanford, California, USA.

²Electrical Engineering Department, Koç University, Istanbul, Turkey.

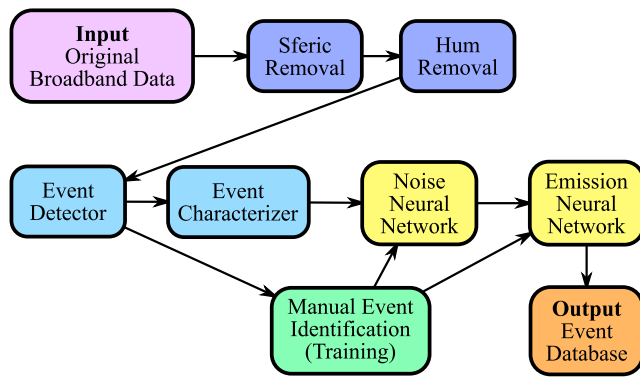


Figure 1. Full emission detector system block diagram.

one of two methods. The first is a simplistic thresholding by frequency, satellite position (for in situ measurements), or other parameters which do not take into account the spectral differences between chorus and hiss [e.g., Meredith *et al.*, 2001, 2004; Smith *et al.*, 2004, 2010]. These potentially suffer from errors in categorization. An alternative and more reliable approach is a by-hand examination of the broadband emissions [e.g., Tsurutani and Smith, 1974; Burtis and Helliwell, 1976; Smith *et al.*, 1996]. However, broadband data is not always available and, even when it is, this procedure can be prohibitively time-consuming.

[6] This paper describes an alternate approach to the problem of distinguishing between chorus and hiss in ground-based broadband ELF/VLF wave data. We use an artificial neural network, which is an example of a machine learning technique which must first be “trained” by the user with example data before it is functional. After being trained with a representative sample of events, which have been marked as either “noise”, “chorus”, or “hiss”, the neural network is able to operate on an arbitrarily large set of data and automatically sort events into the appropriate categories. The full system described herein consists of three broad sections: (1) cleaning the source broadband data of common sources of interference, (2) detecting “events” which, before categorization, may be either emissions or noise, and (3) categorizing the detected events as noise, chorus, and hiss. In this paper, we use the term “event” to refer to events output from the event detector which have not yet been categorized as noise, chorus, or hiss, and the term “emission” to refer to an event which has been categorized as either chorus or hiss (or is otherwise a priori known to be either of these emissions).

[7] The emission detector was run on 10 continuous years of broadband data from Palmer Station, Antarctica ($L = 2.4$, 50°S invariant latitude), from May 2000 through May 2010. We present several results from this analysis, including the occurrence rates of chorus and hiss over the course of the entire solar cycle as well as on a monthly basis, averaged over the 10 years of data.

2. Automated Emission Detection

[8] Palmer Station is located on Anvers Island, near the tip of the Antarctic peninsula, at 64.77°S , 64.05°W , with

IGRF geomagnetic parameters of $L = 2.4$, $\Lambda = 50^\circ\text{S}$ invariant latitude, and magnetic local time (MLT) = UTC - 4.0 at 100 km altitude. The Palmer ELF/VLF receiver records broadband ELF/VLF data at 100 kilosamples per second using two cross-loop magnetic field antennas, with 96 dB of dynamic range. This analysis uses the North/South channel exclusively, it being the less subjectively noisy of the two channels; this has the additional effect of focusing Palmer’s viewing area more tightly to its magnetic meridian than if both channels were used. Data records used in this study are 10-s broadband data files, sampled at a rate of 100 kilosamples/s, beginning every 15 min at 5, 20, 35, and 50 min past the hour, 24 h per day. The 10-s data record length was chosen because we found that it is the optimal length for manually identifying events on broadband spectrograms. The start time of a data record is referred to as a “synoptic epoch”.

[9] The automated emission detector consists of three broad steps: (1) cleaning of the source broadband data of common sources of interference (discussed in section 2.1), (2) detection of “events” and characterization of their properties (discussed in sections 2.2 and 2.3), and (3) automatic categorization of detected events as noise, chorus, and hiss, using a sequential pair of complementary neural networks (discussed in section 2.5). The properties of the neural networks are initially determined using a training set of events which have been categorized by a human operator (discussed in section 2.4), after which the neural networks operate autonomously. These steps are illustrated in the system block diagram in Figure 1.

2.1. Removal of Sferics and Hum

[10] One inevitable disadvantage of ground-based data versus that gathered via in situ measurements is that they are subject to certain sources of terrestrial interference which are not found in appreciable quantities in space. The two most prevalent and debilitating for automated detection are sferics, which are the broadband electromagnetic impulses from terrestrial lightning flashes, and hum, which is the anthropogenic parasitic radiation from terrestrial power distribution systems. Both of these noise sources are mitigated prior to event detection.

[11] We first discuss the method of automatically removing sferics from broadband data via a two-step process of sferic identification, followed by sferic removal. The sferic identification process is discussed first and follows the technique of Said [2009, p. 110]. Sferics propagating in the Earth-ionosphere waveguide from larger propagation distances have maximal energy roughly concentrated near 9–13 kHz, which is the result of the convolution of their original radiated spectrum with the attenuation characteristics of the Earth-ionosphere waveguide. Therefore the first step of sferic identification is to apply a passband filter between 5 and 15 kHz to the original full-spectrum 100-kilosamples/s broadband data. The frequency 5 kHz is above the typical observed frequencies for chorus and hiss at Palmer, so this frequency range is unlikely to contain spectral information from those emissions (which may result in “false positives” during sferic detection). The filtered signal is then squared (to increase contrast) and decimated to a sampling frequency of 6 kHz. The absolute value of the resulting signal is the

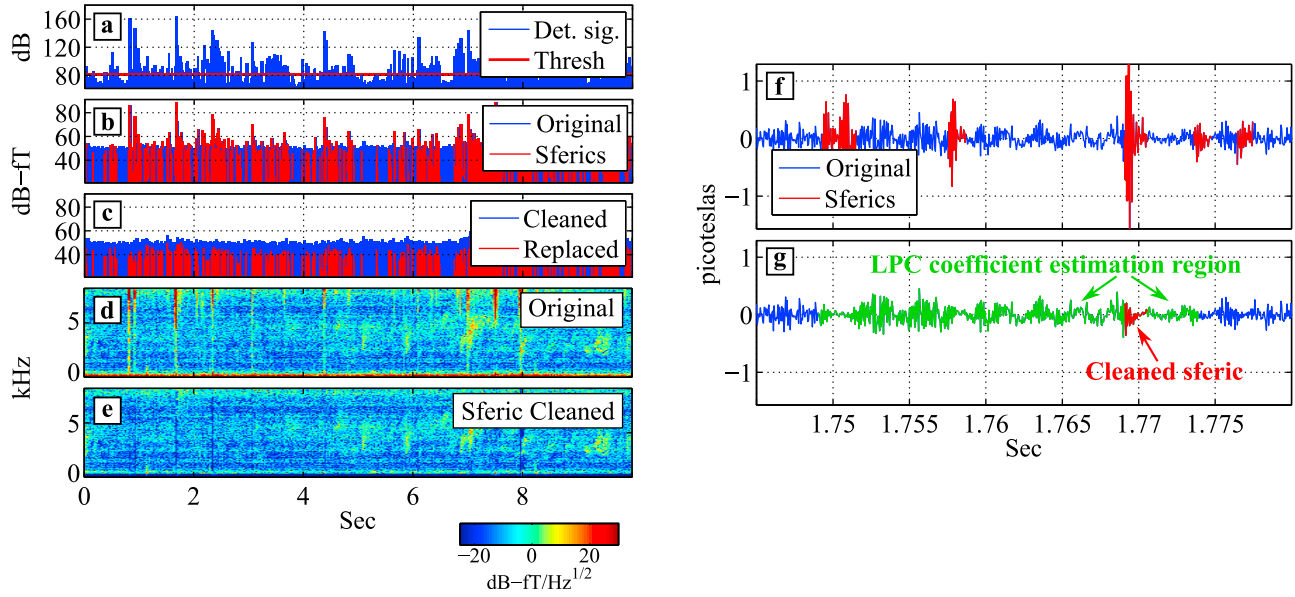


Figure 2. Sferic removal procedure shown with 10 s of Palmer data from 22 April 2001, 1150:05 UTC. (a) A detection signal is constructed from data between 5 and 15 kHz, where sferic strength is maximized. Components of this detection signal above a threshold are labeled as sferics. (b) Time domain data, sampled at 20 kilosamples/s. Detected sferics are colored red, and original data is colored blue. (c) Time domain data after sferic removal. The modified sferic locations are marked in red, as above, and their amplitude is now below that of the background data. (d) A spectrogram of the original data, showing a chorus emission that is corrupted by sferics and hum. (e) The same spectrogram after sferic removal. (f) A zoomed-in portion of 35 ms of time domain data from Figure 2b. As before, detected sferics are marked in red against the blue background data. The amplitude scale is now linear. (g) Same data as above, after cleaning. A cleaned sferic of interest is shown in red. Data from 20 ms before to 5 ms after the sferic are used in generating the LPC coefficients for interpolation over the sferic and are shown in green.

“detection signal”. The detection signal is then thresholded, and any contiguous time points during which the detection signal is above the threshold are labeled as sferics. A threshold of $0.01\sigma_d$, where σ_d is the standard deviation of the detection signal, has been found to work well in practice. Detected sferics of shorter duration than 1 ms are extended to have duration of at least 1 ms. In addition, any discrete sferics which are closer together than 1.5 ms are combined into a single sferic. The output of sferic detection is only the time indices of the data which contain sferics; the original data has not yet been altered up to this point. Figure 2 shows the process of sferic detection and removal for an example 10-s segment of Palmer data. Figure 2a shows the detection signal in blue and the threshold at $0.01\sigma_d$ in red.

[12] After sferics have been identified, the cleaning process begins with the unaltered original broadband data. This data is decimated to a sampling frequency of 20 kilosamples/s, for a maximum observable frequency of 10 kHz. This both isolates the frequencies over which chorus and hiss are typically observed and increases processing speed due to the reduced data volume. Figure 2b shows the time domain data after decimation with detected sferics labeled in red.

[13] Before sferic removal takes place, an IIR highpass filter with a cutoff frequency of 375 Hz is applied to the data to mitigate issues arising from sferic slowtails, i.e., the ELF,

high-amplitude components of sferics that propagate below ~ 500 Hz in the transverse electromagnetic (TEM) mode in the Earth-ionosphere waveguide. Because the upper frequency cutoff of slowtails is variable, and chorus and hiss emissions are often seen at ELF frequencies which overlap the slowtail frequency range, the cutoff frequency of the highpass filter is chosen to be a compromise between eliminating most of the slowtail energy while preserving as much of the full bandwidth as possible in which to detect emissions.

[14] Sferics are mitigated by first zeroing out samples that have been identified as sferics, and then interpolating over those samples. By interpolating over the sferics instead of simply zeroing them out and smoothing the result, we attempt to maintain continuity of the underlying signals, thereby preserving their spectral properties which are used when characterizing events (section 2.3). Interpolation is accomplished using linear-predictive coding (LPC) with an autoregressive (AR) model of the signal [Godsill and Rayner, 1998, sec. 5.2.2]. Under the AR model, a given sample of the signal is modeled as a linear combination of prior samples, as

$$x_n = \sum_{i=1}^P a_i x_{n-i} + e_n \quad (1)$$

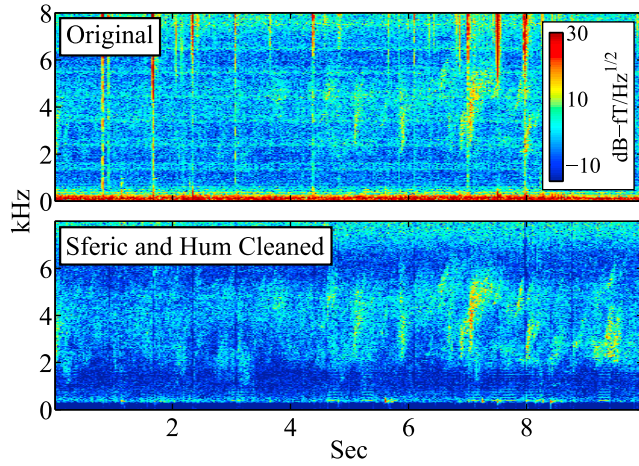


Figure 3. Result of removing both sferics and hum from data. This is the same 10-s broadband data segment as in Figure 2. In the cleaned data, it is much easier to identify the chorus emission between 2 and 6 kHz.

where x_n represents a sample at discrete time index n , P is the order of the AR process, the P coefficients a_i are the AR coefficients, and e_n is the error. Define the matrix \mathbf{A} as

$$\mathbf{A} = \begin{bmatrix} -a_P & \dots & -a_1 & 1 & 0 & 0 & \dots & 0 \\ 0 & -a_P & \dots & -a_1 & 1 & 0 & \dots & 0 \\ \vdots & \ddots & \ddots & \ddots & \ddots & \ddots & \ddots & \vdots \\ 0 & \dots & 0 & -a_P & \dots & -a_1 & 1 & 0 \\ 0 & \dots & 0 & 0 & -a_P & \dots & -a_1 & 1 \end{bmatrix}. \quad (2)$$

Then, the error sequence can be expressed as

$$\mathbf{e} = \mathbf{A}\mathbf{x}. \quad (3)$$

[15] For a given sferic, we create three segments of data: \mathbf{x}_u is the detected sferic, which has been zeroed out and now consists of unknown values to be estimated, \mathbf{x}_b is 20 ms of data before the first sample of \mathbf{x}_u , and \mathbf{x}_a is 5 ms of data after the last sample of \mathbf{x}_u . Because sferics are cleaned sequentially, \mathbf{x}_b is known to be free of sferics, while \mathbf{x}_a is not. The entire data segment of interest is then given by

$$\mathbf{x} = \begin{bmatrix} \mathbf{x}_b \\ \mathbf{x}_u \\ \mathbf{x}_a \end{bmatrix}. \quad (4)$$

We can also express the known and unknown values of \mathbf{x} as $\mathbf{x}_k = [\mathbf{x}_b^T \mathbf{x}_a^T]^T$ and \mathbf{x}_u , respectively.

[16] The entire sequence \mathbf{x} is used to estimate the LPC coefficients, via the LPC function in the Matlab software package, including \mathbf{x}_u which consists of all zeros. Although it may seem that only \mathbf{x}_b should be used to estimate the LPC coefficients, since \mathbf{x}_u consists of all zeros and \mathbf{x}_a may contain sferics, in practice, there is negligible difference in the results. The risk of including sferics in the LPC estimation via \mathbf{x}_a is mitigated by ensuring that it is significantly smaller (5 ms versus 20 ms) than the sferic-free portion of the estimation, \mathbf{x}_b . For reference, at the implemented sampling

rate of 20 kilosamples/s, the 25 ms of data used in LPC coefficient estimation consists of 500 samples.

[17] To estimate the missing data \mathbf{x}_u , partition the columns of \mathbf{A} into columns for known \mathbf{A}_k and unknown \mathbf{A}_u indices of \mathbf{x} such that

$$\mathbf{e} = \mathbf{A}_k \mathbf{x}_k + \mathbf{A}_u \mathbf{x}_u. \quad (5)$$

[18] The objective is to obtain an estimate of \mathbf{x}_u given \mathbf{A} and \mathbf{x}_k , which minimizes the mean squared error, which is proportional to $\mathbf{e}^T \mathbf{e}$. This is achieved by setting \mathbf{e} to zero and solving for \mathbf{x}_u , as

$$-\mathbf{A}_k \mathbf{x}_k = \mathbf{A}_u \mathbf{x}_u. \quad (6)$$

Assuming that \mathbf{A}_u is skinny and full rank, the traditional least squares solution is

$$\mathbf{x}_u = -(\mathbf{A}_u^T \mathbf{A}_u)^{-1} \mathbf{A}_u^T \mathbf{A}_k \mathbf{x}_k. \quad (7)$$

The solution for \mathbf{x}_u gives the data sequence with which to replace the zeroed-out sferic. This process is repeated sequentially for every detected sferic in the data.

[19] Figure 2c shows the result of the sferic removal process in the time domain. Energy in the samples that contained sferics has been reduced to below the background levels of the signal. Figures 2d and 2e show spectrograms of the signal before and after sferic removal. Although some broadband “nulls” have been introduced in the place of more powerful sferics (which generally have a longer extent in time than less powerful ones), the majority of low-amplitude sferics are removed without nulls and there is no broadband ringing as would have resulted from simply zeroing-out the sferics in the time domain data. Given that events are detected based on their spectrum (section 2.2), these occasional nulls are far more tolerable than either the original sferics or nulls for every sferic.

[20] Figure 2f shows a zoomed-in portion of 35 ms of the time domain data from Figure 2b, highlighting several detected sferics, where now the amplitude scale is linear instead of logarithmic (1 picotesla = 60 dB-fT). Figure 2g shows in green the range of data used for estimating the LPC coefficients for the given cleaned sferic, shown in red.

[21] Another noise source observed at Palmer is hum, which consists of parasitic leakage of 60-Hz noise and its harmonics from the Palmer Station power distribution system. Hum is mitigated using the technique of *Cohen et al.* [2010]. Hum frequency is estimated via the “quadratic interpolation” method using odd hum harmonics 7–31 (420, 540, ..., 1860 Hz). Odd harmonics are chosen because they are significantly more intense than even harmonics at Palmer. The lower frequency of 420 Hz is the first odd harmonic in the passband of the slowtail highpass filter, and hum is usually no longer significant at Palmer above the upper frequency of 1860 Hz. After its frequency has been estimated, hum is removed via the “least squares estimation” method. This process is repeated in intervals of 200 ms to account for a potentially slowly changing hum frequency.

[22] Figure 3 shows spectrograms of the same data segment from Figure 2 before and after both sferics and hum are removed. Contrast of the chorus emission between 2 and

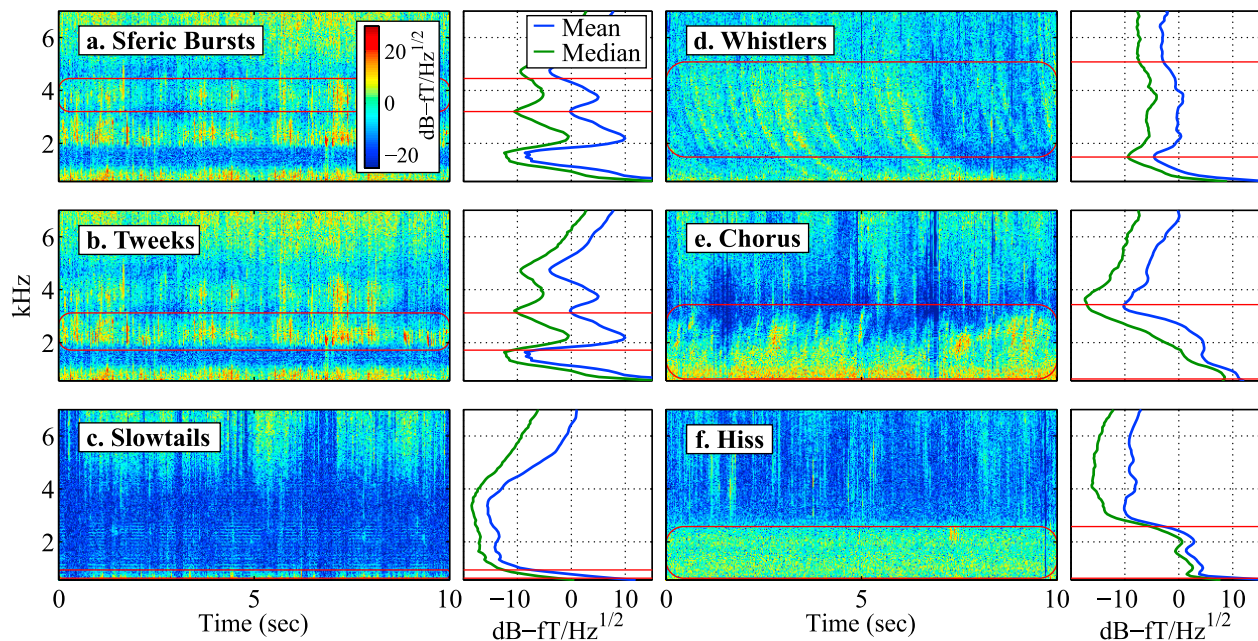


Figure 4. Examples of common types of events as output by the event detector. Spectrograms for each type of event are shown, along with the associated periodogram (blue line) and mediogram (green line) for that data segment. The detected event is indicated with a red box. Although the majority of high-amplitude sferics are removed in the broadband cleaning process prior to event detection, sferic bursts are not removed in this manner and may be detected as events. Similarly, tweeks and slowtails are not removed by the sferic removal process due to their nonimpulsive nature. Whistlers are a common broadband emission at Palmer and are of scientific interest for a variety of reasons, but they are not used in this study and are therefore considered noise. Chorus and hiss are the emissions of interest in this study.

6 kHz is greatly enhanced after cleaning, emphasizing the usefulness of this preprocessing step before initiating the actual detection of emissions.

2.2. Event Detection

[23] Once data is cleaned, events may be detected which are candidates for being classified as chorus or hiss. In contrast to transient electromagnetic phenomena from lightning, such as sferics and whistlers, and other transient emissions, such as periodic and quasiperiodic emissions [e.g., *Helliwell*, 1965, pp. 206–207; *Sazhin and Hayakawa*, 1994], chorus and hiss emissions may persist for minutes or hours with similar spectral characteristics over their entire duration. Thus when examining individual 10-s records for each synoptic epoch, we are interested only in events whose power spectral densities (PSDs) are approximately constant throughout the 10-s record. It is natural then to detect events and their associated bandwidth using the one-dimensional frequency spectrum of the 10-s record, instead of the two-dimensional spectrogram. A standard method of estimating the spectrum of a signal is via the Welch periodogram [*Welch*, 1967], which, assuming the same windowing and Fourier transform parameters, can be thought of as the average of a spectrogram matrix over time. However, the Welch periodogram in its usual form is not adequate for our purposes. Despite the sferic removal discussed in section 2.1, certain types of high-amplitude, longer-duration impulsive signals may remain in the cleaned data, such as tweeks (the highly dispersed components of sferics near the Earth-

ionosphere waveguide cutoff frequencies) and lightning-generated whistlers (sferic energy which has escaped into the magnetosphere, become dispersed in the magnetospheric plasma, and returned through the ionosphere in the opposite hemisphere). Though these transient signals may last for less than 1 s, their high amplitude may result in a contribution to the PSD of the Welch periodogram which is disproportionate to their duration. This may in turn mask a continuous chorus or hiss emission with a lower PSD at the same frequency. To mitigate this problem, we discard the Welch periodogram, which is formed from the mean of the columns of a spectrogram, in favor of what we term the “Welch mediogram” (or more simply, “mediogram”) formed from the median of the columns of a spectrogram. Like any median filter, the mediogram has the property that it emphasizes spectral content which is persistent in time and deemphasizes transient signals.

[24] Six common types of events are shown in Figure 4, where the full 10-s record for each synoptic epoch is shown and the event is marked with a red box. Note that, although both the periodogram (blue, “mean”) and mediogram (green, “median”) PSDs are shown, only the mediogram is used in event detection. The most common sources of noise are those from lightning, including sferic bursts from intracloud lightning (which appear in broadband data as many closely spaced low-amplitude sferics), tweeks, slowtails (Figures 4a, 4b, and 4c) and whistlers (Figure 4d). The events of interest are chorus and hiss (Figures 4e and 4f). Although periodic and quasiperiodic emissions do occur at Palmer’s invariant

latitude ($\Lambda = 50^\circ\text{S}$) (see, e.g., observations at Seattle, $\Lambda = 54^\circ\text{N}$, Dunedin, $\Lambda = 51^\circ\text{S}$, Norwich, $\Lambda = 55^\circ\text{N}$, and others [Helliwell, 1965, section 7.1]), they are generally not detected at Palmer due to their relative rarity compared to chorus and hiss, and also due to their transient behavior, which is deemphasized by the mediogram.

[25] The arithmetic difference between the PSDs of the Welch periodogram and the Welch mediogram is generally a good measure of the “impulsiveness” of a given event. This is illustrated particularly well in the hiss event in Figure 4f, where above ~ 3 kHz, there is a large difference between the mediogram and periodogram PSD due to impulsive sferics, while below ~ 3 kHz, the difference is minimal due to the constant-PSD hiss emission.

[26] As mentioned, sferic removal is only effective on the short-time impulsive sferics themselves. It does not remove any other products of terrestrial lightning. Fortunately, two of the most prevalent noise sources, namely sferic bursts and slowtails (Figures 4a and 4c), have fairly predictable spectrums. Additionally, owing to the intensity of these noise sources, it is infeasible to find emissions in the same frequency band. Therefore the first step of the event detection process is to determine the frequency extents of sferic bursts and slowtails in a given broadband record and look only for emissions outside of these ranges.

[27] We define the terms “peaks” and “valleys” as the local maxima and minima in the mediogram, respectively. Slowtails dominate the spectrum at low frequencies, from the 375 Hz slowtail highpass filter cutoff to slightly above. Slowtail PSD has its maximum at frequencies below the filter cutoff and rolls off quickly with increasing frequency on a mediogram. An empirically determined reasonable estimate for the slowtail upper cutoff in a given synoptic epoch is one of (1) the frequency of the first (lowest frequency) valley, (2) the first frequency at which the mediogram slope is less steep than -20 dB/kHz, or (3) 600 Hz, whichever is lowest.

[28] The high end of the spectrum is dominated by sferic bursts. Sferic burst energy peaks above the ~ 8 kHz antialiasing filter cutoff, so its PSD tends to rise monotonically up to that cutoff. An empirically determined reasonable estimate of the sferic burst lower cutoff is either (1) the highest frequency at which the mediogram PSD (smoothed over 1 kHz) becomes monotonically increasing up to the antialiasing filter cutoff or (2) 8 kHz, whichever is lowest. We refer to the slowtail and sferic burst cutoffs as the sferic lower and upper cutoffs, respectively.

[29] Between the sferic cutoffs, we then search for events. First, all peaks between the two sferic cutoffs are detected and assumed to be candidates for unique events. Because low-frequency emissions are often seen on the edge of the sferic lower cutoff, the frequency of the sferic lower cutoff is added to the list of peaks (though, owing to the fact that emission and slowtail PSDs reach their maximums below the sferic lower cutoff, it is rarely a true peak). Second, the 3-dB points for each peak, defined as the nearest frequencies above and below each peak at which the mediogram PSD is 3 dB or more below that of the peak, is determined. The width of the peak is then defined as the frequency difference between its two 3-dB points, i.e., the full width at half maximum (FWHM). If either 3-dB point is beyond either sferic cutoff, then the FWHM is defined as twice the

frequency difference between the peak and the remaining 3-dB point. If both 3-dB points are beyond the sferic cutoffs, the peak is discarded. Additionally, peaks which have a FWHM of less than 100 Hz are discarded.

[30] The upper and lower “extents” of each peak are then determined to be the closest frequencies that can be reached from the peak for which (1) the mediogram PSD is at least 9 dB less than the PSD at the peak, or if no such point is found, (2) the frequency of the lowest mediogram PSD between the peak and the respective sferic cutoff, inclusive. Additionally, the extents may not include any mediogram PSDs which are greater than the given peak. The bandwidth of a given peak is then defined as the frequency difference between its upper and lower extents. Peaks with bandwidths less than 300 Hz are discarded. Finally, each peak is checked to determine whether it is contained within the extents of a higher-PSD peak. If so, it is discarded.

[31] Each peak which passes this gauntlet of tests is then labeled as an “event” and is a potential candidate for being categorized as an emission. At this point, events are not yet categorized and may include either chorus, hiss, or noise (i.e., anything other than chorus or hiss).

[32] The relevant metric for the efficacy of the event detector is its missed detection rate, i.e., the percent of chorus or hiss emissions that the event detector fails to identify. In this implementation, there are no false positives from the event detector since those events are discarded using the noise neural network (section 2.5). To evaluate the missed detection rate, we manually examined a subset of synoptic epochs that were processed with the event detector. In 1000 synoptic epochs, we noted 15 chorus or hiss emissions that were not detected by the event detector, primarily as a result of their blending into the sferic cutoffs. To make a concrete statement about the event detector’s missed detection rate, we model each sampled synoptic epoch as an independent Bernoulli trial and test the null hypothesis of the form

$$H_0 : p \leq p_0 \quad (8)$$

where p is the true (unknown) missed detection rate of the detector, and p_0 is a missed detection rate which we say with 95% confidence is greater than the true missed detection rate. To test this hypothesis, the z -score is computed as [Navidi, 2006, sec. 6.3]

$$z = \frac{\hat{p} - p_0}{\sqrt{p_0(1 - p_0)/n}} \quad (9)$$

where $n = 1000$ is the number of trials, and $\hat{p} = 0.015$ is the observed missed detection rate. The P -value of the hypothesis test is then the area to the left of z under the standard normal probability distribution function with mean 0 and standard deviation 1. To reject the null hypothesis at the 5% level, the P value and corresponding normal cumulative distribution function should equal 0.05, which gives $z = -1.65$. Equation (9) can then be solved for p_0 to give $p_0 = 0.023$. Thus we can state with 95% confidence that the missed detection rate of the event detector is less than 2.3%, or conversely, at least 97.7% of emissions are detected.

2.3. Event Characterization

[33] Once events are detected, various scalar characteristics are determined about each event. These characteristics

Table 1. List of Event Characteristics and Units

	Name	Units
1	Year	Years (2000–2010)
2	Day of year	Days (1–366)
3	Peak frequency	Hz
4	Upper cutoff frequency	Hz
5	Lower cutoff frequency	Hz
6	Bandwidth	Hz
7	Max positive mediogram slope	(dB-fT/Hz ^{1/2})/Hz
8	Max negative mediogram slope	(dB-fT/Hz ^{1/2})/Hz
9	Avg mediogram PSD	dB-fT/Hz ^{1/2}
10	Avg periodogram PSD	dB-fT/Hz ^{1/2}
11	Max mediogram PSD	dB-fT/Hz ^{1/2}
12	Max periodogram PSD	dB-fT/Hz ^{1/2}
13	Median power	dB-fT
14	Time to day/night terminator	Hours
15	Burstiness	Hz
16	XC slope	sec/Hz
17	XC correlation coefficient	Unitless (0–1)
18	XC mean value	Unitless (0–1)
19	XC mean standard deviation	Unitless (0–1)

are used as inputs to the neural network, described in section 2.5. Each characteristic is chosen because of the potential that it may have, possibly in conjunction with other characteristics, to aid the neural network in differentiating between different types of events. A total of 19 characteristics are determined for each event; they are summarized in Table 1 and are discussed in more detail below. As many reasonable characteristics were chosen as possible, without an in-depth analysis of the influence of each characteristic on the result.

[34] The year and day of year of the synoptic epoch are included to incorporate seasonal and long-term differences in emission characteristics. The peak frequency, upper cutoff frequency, lower cutoff frequency, and bandwidth are basic parameters for each event and are determined during event detection, described in section 2.2.

[35] Additional emission spectral parameters include the maximum positive and negative mediogram slopes over the course of the emission (measurements of how rigidly band-limited the event is), average mediogram and periodogram PSD (the difference of which is a measure of the impulsiveness of the event), and maximum mediogram and periodogram PSDs. The “median power” is the integral of the mediogram PSD (in fT²/Hz) over the bandwidth of the event. This value is integrated in power space and therefore is different from the event’s average mediogram amplitude, which is averaged in log space and is not multiplied by the bandwidth.

[36] The “time to day/night terminator” is defined as the time from the synoptic epoch to the nearest terminator, either dawn or dusk. If Palmer is in darkness during the synoptic epoch, then this number is positive, otherwise it is negative. This parameter is incorporated because all types of events are more common during darkness; this is a consequence of the lower absorption of the ionosphere during the night that affects both transionospheric propagation and propagation in the Earth-ionosphere waveguide.

[37] The “burstiness” parameter is somewhat more involved and attempts to measure the canonical spectral difference between chorus and hiss, namely that the former is a “bursty” emission (containing discrete structure in time) while the

latter is not. Burstiness is estimated as follows. First, the event is mixed to baseband by multiplying with a cosine at the event center frequency and decimating to a sampling frequency equivalent to the bandwidth of the event. Then, the signal is squared so that it is in units of power and decimated again to a sampling frequency of 100 Hz. Finally, the Welch periodogram is calculated for the signal, and the centroid of the Welch periodogram (for positive frequencies only) is obtained. In this case, the centroid represents the mean frequency of the Welch periodogram, weighted by periodogram amplitude (in units of power) and is a measure of the frequency at which the signal power tends to be concentrated. Signals which are not bursty (such as hiss) will have a spectrum which resembles random noise and will have a centroid near the center of the spectrum, at 25 Hz. Signals which are bursty (such as chorus) will have spectral power concentrated near the low end of the spectrum and will have a centroid lower than 25 Hz (representing a significant amplitude modulation of a few Hz). The centroid is used as the burstiness parameter and has units of Hz.

[38] The four remaining parameters, prefixed with the letters “XC”, represent parameters relating to the cross-correlation of adjacent rows of a signal spectrogram. For each adjacent pair of rows in the spectrogram (corresponding to a pair of frequencies), the cross-correlation is computed. The cross-correlation vector provides a measure of the total correlation between the two rows (given by the peak value of the cross-correlation vector) and the dominant slope of the event in that frequency range (given by the lag of the peak of the cross-correlation). The “XC slope” parameter is calculated as the centroid of the average (over frequency) of all of the cross-correlation vectors, divided by the frequency step of the spectrogram. It is a measure of the dominant slope of the event and has units of s/Hz. The “XC correlation coefficient” is the mean of the amplitudes of each cross-correlation vector at the lag indicated by XC slope and is a measure of the “strength” of that dominant slope, from 0 to 1. “XC mean value” is the mean of all values of all cross-correlation vectors; a higher value indicates a wider range of lags over which correlation is high and suggests thicker event elements in time (e.g., chorus and whistlers) as opposed to thinner ones (e.g., sferics). “XC mean standard deviation” is the mean of the standard deviations of each cross-correlation vector and is a complementary parameter to the XC mean value. Events which tend to have large XC correlation coefficients include whistlers, which have negative slopes, chorus emissions, which usually have positive slopes, and sferics, which usually have slopes near zero. Hiss tends to have a low XC correlation coefficient since its spectrogram rows are random noise and therefore are minimally correlated. Additionally, hiss tends to have an XC slope near zero, since its cross-correlation vectors appear as random noise with centroids near zero lag.

2.4. Construction of the Neural Network Training Set

[39] After the events have been detected and characterized, the next step in the emission detection process is the construction of a training set for the neural network. The set of events included in the training set is a subset of all (uncategorized) events output from the event detector. We use events from 1 day out of every 15 for training, or approximately 24 days per year, for a total of approximately 240 days

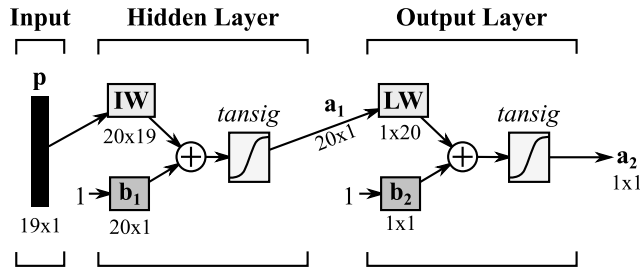


Figure 5. Neural network block diagram. This block diagram describes both the noise neural network and the emission neural network, which are structurally equivalent, but have different weights and biases. The size of each element is indicated by the dimensions below the given element; e.g., **IW** is a matrix with 20 rows and 19 columns.

of training data for the 10-year data set. This cadence is a compromise between having adequate training data and the general tediousness of the training process. The training data used contains 10,013 out of a total of 154,639 events for the 10 years of data used in this study.

[40] Assembly of the training set is simple and repetitive. The human trainer makes use of a graphic user interface which displays a spectrogram for a given event in the training set. The event is highlighted on the spectrogram with a red box. The trainer categorizes the event as either (1) chorus, (2) hiss, (3) an unknown nonnoise emission (which the trainer is unable to categorize as chorus or hiss from the spectrogram), or (4) noise. This process is repeated for all 10,013 events in the training set. In the case of a “mixed” detection with more than one type of event in the same bandwidth (e.g., the relatively common simultaneous whistlers and hiss), the detected event is categorized according to the event with the greater PSD. This decision is made under the principle that the characteristics of the detected event (discussed in section 2.3) are primarily based on the event with the greater PSD (i.e., the dominant constituent of the detected event’s spectrum).

[41] The result of this procedure is a $1 \times 10,013$ vector of “target” values, each of which is either chorus, hiss, unknown emission, or noise. Independently, the automated event characterizer determines the characteristics for each event, resulting in a $19 \times 10,013$ matrix of input values. Note that the input values are not used by the trainer in assembling the training set; only the event time, frequency range, and broadband spectrogram are used.

2.5. Neural Network Implementation and Training

[42] The training set is then in a suitable format for being used to train a neural network. The Matlab Neural Network Toolbox is used for all neural network operations. Two completely separate neural networks are implemented: a neural network to distinguish between emissions and noise, which we refer to as the “noise neural network”, and a neural network to distinguish between chorus and hiss, which we refer to as the “emission neural network”. A neural network is capable of having an arbitrary number of outputs, and we could have created a single neural network to distinguish between chorus, hiss, and noise. However, we choose to use a sequence of two neural networks so that they

may be trained using different training sets, as is explained later.

[43] Both the noise and emission neural networks are known in Matlab as “pattern recognition networks” and have identical structure, shown in Figure 5. Each neural network consists of a 20-neuron hidden layer followed by a single-neuron output layer and takes as input the 19-value event characteristics vector (**p**) described in section 2.3. Trial and error has shown that 20 neurons in the hidden layer is sufficient to achieve reasonable performance for both networks. Each neuron in the hidden layer contains a single weight for each of the 19 inputs and a single bias. The resulting matrix of weights (**IW**) is a 20×19 matrix, and the resulting vector of biases (**b**₁) is a 20×1 vector. Similarly, the single neuron in the output layer contains 20 weights, one for each output of the 20 neurons from the hidden layer and a single bias. The resulting matrix of weights (**LW**) is a 1×20 matrix, and the resulting bias (**b**₂) is a scalar. The transfer function for both layers is the hyperbolic tangent sigmoid function (tansig), which transforms unbounded input into bounded output in the range $[-1, +1]$. The output of the output layer is further thresholded so that the final output of the network is a boolean true/false value (corresponding to emission/noise and hiss/chorus, respectively). In theory, the threshold may be set to preferentially maximize true positives or minimize false positives, but in practice, it is left at the point which minimizes the total number of detection errors. The output of the hidden layer is given by

$$\mathbf{a}_1 = (\mathbf{b}_1 + \mathbf{IW}\mathbf{p}) \quad (10)$$

and the output of the output layer before thresholding is given by

$$\mathbf{a}_2 = (\mathbf{b}_2 + \mathbf{LW}\mathbf{a}_1). \quad (11)$$

[44] The training set used for the noise neural network is the full training set (10,013 events), with targets set to 0 if the event is noise and 1 if the event is any type of emission other than noise. The training set used for the emission neural network is only those events in the full training set which have been categorized as chorus or hiss (2453 events); unknown emissions and noise are discarded from the training set for this neural network. The principle behind this is that, once noise events are eliminated with the noise neural network, the emission neural network will categorize all remaining events, including those which would be categorized by the trainer as unknown emissions, as either chorus or hiss. In this way, the neural network is expected to outperform the trainer by categorizing emissions based on their similarity, in the 19-dimensional property space shown in Table 1, to events which the trainer is able to categorize.

[45] For example, let us say that the human trainer categorizes emission A as chorus and emission B as hiss but is unable to make a decision about emission C. The neural network would then categorize emission A as chorus, based on its similarity to other known chorus emissions (previously categorized by the trainer), and emission B as hiss, based on its similarity to other known hiss emissions. Finally, it would examine the characteristics of emission C;

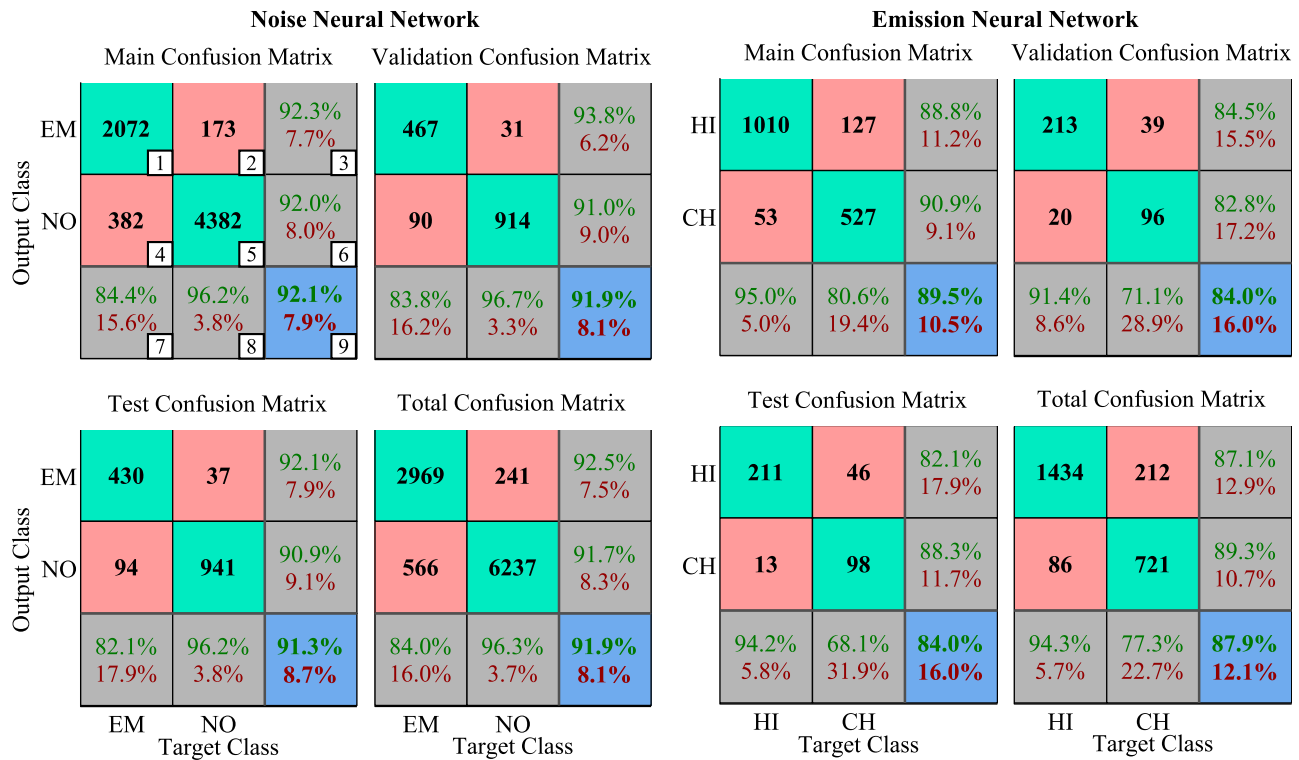


Figure 6. Neural network confusion matrices for training of (left) the noise neural network and (right) the emission neural network. Each training set is split into three subsets: the “main” set (70% of inputs), the “validation” set (15% of inputs), and the “test” set (15% of inputs). The “total” set represents the sum of all three sets. In the noise neural network, the labels “EM” and “NO” mean emissions and noise, respectively, and in the emission neural network, the labels “HI” and “CH” mean hiss and chorus, respectively. The boxes in each confusion matrix are described with respect to the noise main confusion matrix in the upper left. Squares 1 and 5 (green background) represent the number of neural network outputs which matched the targets, and squares 2 and 4 (red background) indicate the number of neural network outputs which failed to do so. Squares 7 and 8 represent the percent of each target class which were (upper green number) and were not (lower red number) categorized correctly. Squares 3 and 6 represent the percent of each *output* class which were and were not categorized correctly. Square 9 (blue background) indicates the total percent of outputs which matched their targets (correct detections, upper green number) and those that did not (lower red number).

if they more closely resembled those of known chorus emissions, emission C would be categorized as chorus, and if they more closely resembled those of known hiss emissions, emission C would be categorized as hiss. In this way, the neural network is capable of making intelligent decisions about event categorization based on information and processing power which are not readily available to the trainer.

[46] Both neural networks are trained using the scaled conjugate gradient backpropagation method [Möller, 1993] with initial weights and biases chosen via the Nguyen-Widrow initialization algorithm [Nguyen and Widrow, 1990]. The training set for each neural network is split into three groups: the “main” set (70% of values), the “validation” set (15% of values), and the “test” set (15% of values). The backpropagation training procedure is performed only with the main set. The validation set is used to improve the generalization of the neural network via early stopping as follows. During training, the error of the main set (defined as the mean squared error between the targets and the current outputs of the network) decreases monotonically

and, initially, so does the error of the validation set. However, at a certain point, the error of the validation set stops decreasing due to overfitting of the neural network to the main set. The training is halted after the error of the validation set fails to decrease for six iterations. In contrast, the test set is a completely independent measure of the effectiveness of training and is not used in the training at all.

[47] The results of training are shown via the confusion matrices in Figure 6, and instructions on interpreting the confusion matrices are contained in the caption. It can be seen that the noise neural network, on the left of Figure 6, correctly categorizes 91.9% of the input data and shows no signs of overfitting, as seen from the fact that the total success rates of the main and test sets are very similar (92.1% versus 91.3%). The emission neural network performs nearly as well, correctly categorizing 87.9% of emissions, but with some symptoms of overfitting, as seen from the fact that the percent of correct detections for the main set (89.5%) is significantly higher than that of the test and validation sets (both 84.0%). However, when we tried to

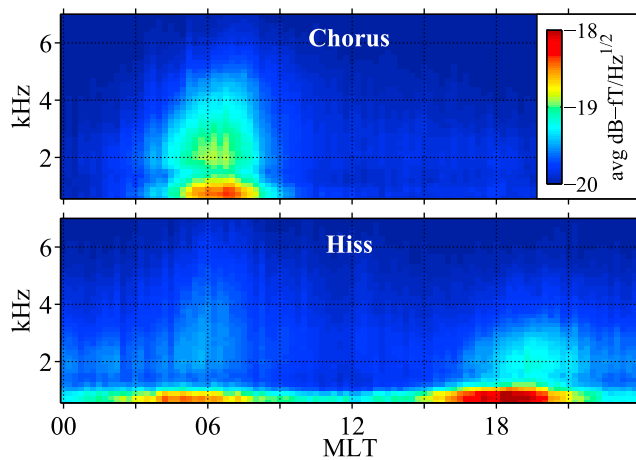


Figure 7. Cumulative spectrograms for chorus and hiss computed over the entire 10-year data set. The cumulative spectrogram is effectively a plot of normalized occurrence for chorus and hiss, weighted by emission PSD, as a function of frequency and local time. Chorus is observed exclusively in the dawn sector. Hiss is observed at all local times, with peaks near dawn and dusk. Additional higher-frequency structure for hiss is observed in the dusk sector.

reduce overfitting by reducing the number of neurons in the hidden layer, the number of correct detections decreased for all three sets. Therefore we tolerate this mild overfitting and accept the fact that the correct detection rate of the emission neural network is expected to be closer to the test and validation rates of 84.0% than the total rate of 87.9%.

[48] Once the neural network has been trained, it is ready to be used on the full catalog of 154,639 detected events over the 10 years of data for this study. Initially, all events are passed through the noise neural network and are categorized as either noise or emissions. All noise events are discarded. All emission events are then passed through the emission neural network, and they are further categorized as either chorus or hiss. The end result is a database of all chorus and hiss emissions detected over the course of this study, including time, frequency, amplitude, and other characteristics from section 2.3. From this database, many different statistics may be determined about chorus and hiss emissions observed at Palmer, a small subset of which is discussed in section 3.

2.6. Algorithm Speed

[49] All aspects of the emission detector are implemented in Matlab Version 2010a. The sferic removal, hum removal, event detection, and event characterization steps are run in parallel using the Matlab parallel computing toolbox with eight simultaneous threads on a Dell PowerEdge R710 rack-mount server with two quad-core Intel Xeon X5550 processors with 8 MB of cache and 16 GB of system RAM. The median time for cleaning one day of data (consisting of a total of 960 s of broadband data from four 10 s data segments per hour) is 234 s. The median time for detecting and characterizing events for one day of data is 16 s.

[50] The neural networks are run on a workstation with an AMD Athlon 64 X2 4200+ dual-core processor with 512 kB

of cache and 4 GB of system RAM. The total time required for the human trainer to create the training set by manually categorizing emissions is approximately one work week. The time required to run the training algorithm on the neural networks and to run the neural networks on the detected events for the entire 10-year data set is less than 5 min.

[51] If only the CPU-bound cleaning and event detection/characterization steps are considered, the chorus/hiss detection system runs at a rate of 350x real time on modern server hardware, assuming four 10-s data segments sampled per hour. If data were sampled continuously, with 360 10-s data samples per hour, the speed would drop to 3.8x real time. In the future, the detection system may be easily implemented in a real time setting at field sites using standard workstation hardware. However, in a real time setting, it would be necessary to periodically add current data to the training set and retrain the network, in the event that site conditions change over time (for example, due to solar cycle variations or changes in system calibration).

3. Solar Cycle Variation of Emissions

[52] The first property of chorus and hiss which we investigate using the emission database is the most common frequency and time ranges for emission occurrence at Palmer. This is visualized using the “cumulative spectrogram” approach described by *Golden et al.* [2009, sec. 2.2]. The cumulative spectrogram is the sum, in log space, of the average mediodiagram amplitude of each emission, divided by the number of available data files for each synoptic epoch. This is effectively a plot of normalized emission occurrence, weighted by emission PSD, with respect to frequency and local time.

[53] Cumulative spectrograms of chorus and hiss emissions from May 2000 through May 2010 are shown in Figure 7. Figure 7 may be compared with *Golden et al.* [2009, Figure 5], though, in Figure 7, we have broken down chorus and hiss in a different way. In particular, when chorus and hiss appear in the same broadband record, regardless of whether they appear in the same or different frequency bands, *Golden et al.* [2009] labeled that entire broadband record as “chorus with hiss”. In contrast, in this study, we independently label multiple emissions in a given broadband record if they occur in different frequency bands. Additionally, we label a given bandlimited emission as “chorus” if it contains chorus-like features, regardless of background hiss in the same frequency band, in light of the fact that the background hiss may simply be an artifact of magnetospheric or subionospheric multipath of the original chorus emission. *Golden et al.* [2009] examined only one year of data, 2003, completely by hand. The similarity then of the automated results from this study to the manual results from *Golden et al.* [2009] are an excellent verification of the automated algorithm (though it should be noted that the same human trainer was used for manual emission identification in both studies, and there may be small systematic biases).

[54] Consistent with other ground studies of chorus [*Storey*, 1953; *Allcock*, 1957; *Pope*, 1957, 1960] and hiss [e.g., *Laaspere et al.*, 1964] at similar geomagnetic latitudes, Figure 7 shows that chorus is essentially restricted to the dawn sector at Palmer at frequencies up to ~6 kHz, while hiss appears at all local times below ~1 kHz, peaking in occurrence in the dawn and dusk sectors. A component of hiss is also seen up to

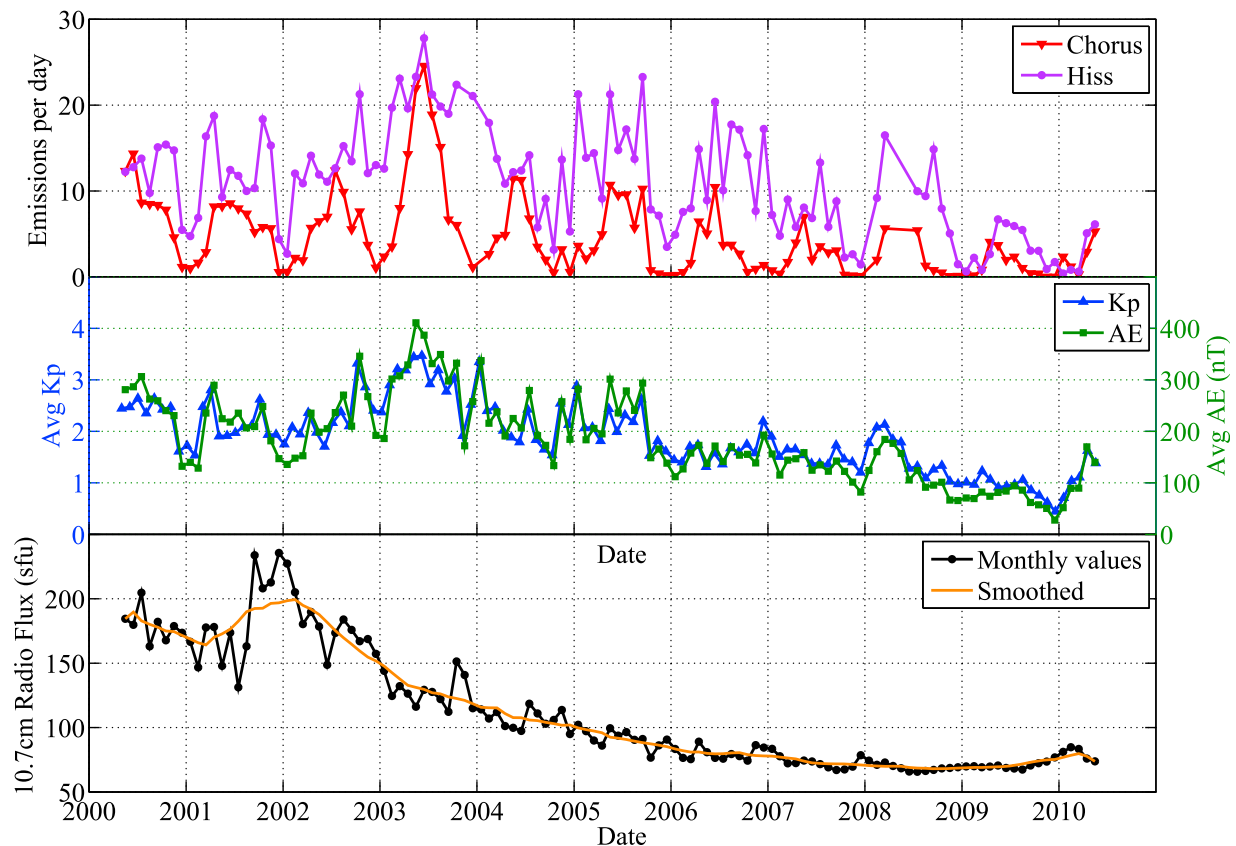


Figure 8. (top) Chorus and hiss occurrence rate, (middle) average K_p and AE indices, and (bottom) solar 10.7-cm radio flux for the entire data set, plotted with a monthly cadence. The 12-month smoothed average of the 10.7-cm radio flux is also plotted as an orange line. Chorus and hiss occurrence is well-correlated with geomagnetic activity in a given month, though neither emission occurrence nor geomagnetic activity is particularly well-correlated with radio flux. In the plot of emission occurrence, months with fewer than 12 full days of data (fewer than 1152 synoptic epochs) have been discarded.

~4 kHz in the dusk sector between 1600 and 2200 MLT [Vershinin, 1970; Carpenter *et al.*, 1975; Hayakawa *et al.*, 1988]. Golden *et al.* [2009] hypothesized that the observed dawn hiss may be partially caused by chorus [Santolik *et al.*, 2006; Bortnik *et al.*, 2008] while the observed dusk hiss may be partially caused by terrestrial lightning [Sonwalkar and Inan, 1989; Draganov *et al.*, 1992; Green *et al.*, 2005; Meredith *et al.*, 2006].

[55] We also break chorus and hiss occurrence down into a count of average number of emissions per day with a monthly cadence over the course of the entire data set. These occurrence rates are shown in Figure 8 (top), along with monthly average K_p and AE indices (Figure 8, middle) and the 10.7-cm solar radio flux from Penticton, British Columbia, Canada (Figure 8, bottom). Two main trends can be seen in the occurrence rates in Figure 8 for both chorus and hiss. First, there is a variation in emission occurrence with year, generally declining from 2000 through 2010 with the exception of 2003, a particularly disturbed year. This corresponds to the decline of solar cycle 23 (as indicated by the decline in 10.7-cm radio flux) and the monthly average K_p and AE values over that range, consistent with the known control of chorus and hiss by geomagnetic activity [e.g., Storey, 1953; Laaspere *et al.*, 1964; Meredith *et al.*, 2001,

2004]. Second, there is a variation in emission occurrence with season, generally peaking in austral winter (June, July, and August) and reaching a minimum in austral summer (November, December, January) due to variations in ionospheric density and absorption that result from seasonal variations in solar illumination [e.g., Helliwell, 1965, sec. 3.8–3.10]. The correlation of geomagnetic activity and, correspondingly, emission occurrence with 10.7-cm radio flux is very weak, and the plot of 10.7-cm radio flux is simply meant to illustrate the phase of the solar cycle.

[56] The solar-cyclical and seasonal trends of emission occurrence can be explored in more detail by focusing individually on the yearly and monthly variation of emissions. Figure 9 (top) shows histograms of chorus and hiss occurrence versus year averaged over all months (left) and occurrence versus month averaged over all years (right). Figure 9 (bottom) shows the K_p and AE indices averaged over the same periods. Note that we have only averaged over synoptic epochs for which we have Palmer data from May 2000 through May 2010, so the 2000 and 2010 averages are only over partial years.

[57] The yearly occurrence rates shown in Figure 9 (left) show a strong correlation with the average K_p and AE values for a given year, indicating strong dependence for both

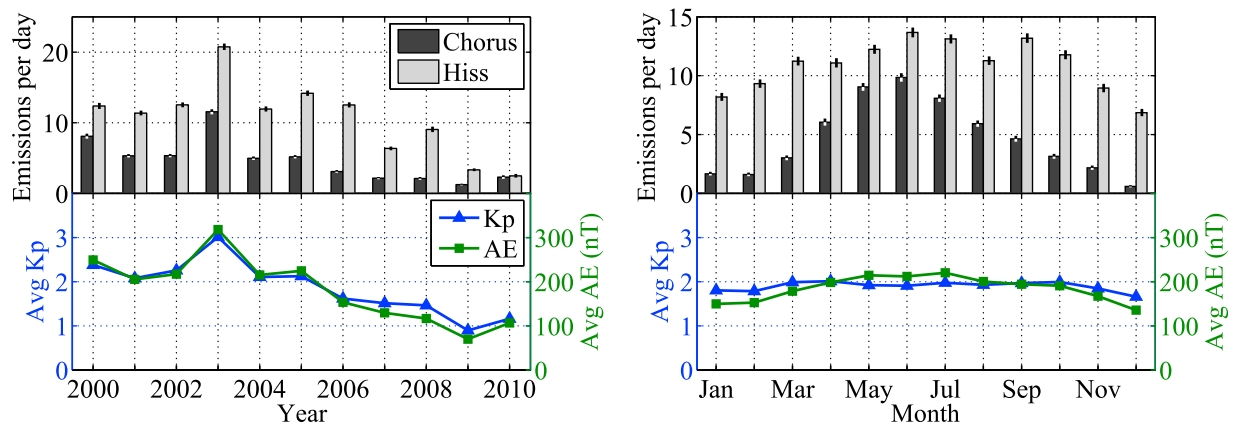


Figure 9. (left) Histogram of chorus and hiss occurrence rate by (top) year and (bottom) average K_p and AE indices. The chorus and hiss occurrence rates naturally follow the average K_p and AE in a given year. (right) Histogram of chorus and hiss occurrence by (top) month and (bottom) average K_p and AE indices. The seasonal variation of hiss is at least partially affected by the mild seasonal variation of geomagnetic activity, while the seasonal variation of chorus is primarily dependent on the seasonal variations of ionospheric absorption due to changing solar illumination. Error bars shown are 95% confidence intervals.

emissions on the geomagnetic disturbance level. The general trend of decreasing occurrence with increasing year is seen, consistent with the decline of K_p and AE in later years coinciding with the waning of solar cycle 23. The obvious exception is 2003, which saw significantly more disturbed geomagnetic conditions than surrounding years. This corresponds to a doubling of chorus occurrence in this year versus 2002 and 2004 and a near-doubling in hiss occurrence versus those same years.

[58] The decline of emission occurrence frequency with waning solar cycle is in contrast to the results of *Smith et al.* [2010], who saw no obvious correlation of average receiver amplitude with sunspot number at the higher-latitude Halley Station ($L = 4.5$, 61.8°S invariant latitude). The lack of correlation observed by *Smith et al.* [2010] may have been due to a variety of factors, including (1) the poor correlation of sunspot number with geomagnetic activity, (2) the corrupting influence of terrestrial lightning in their data, (3) the fact that Halley is on the Antarctic coast and therefore emissions propagating in the Earth-ionosphere waveguide from the Antarctic continent suffer greater attenuation over the Antarctic ice than do emissions observed at Palmer, which primarily propagate over seawater, or (4) simply the fact that Halley is located at a significantly higher L -shell than Palmer and tends to observe a somewhat different set of emissions.

[59] The monthly occurrence rates shown in the right panels of Figure 9 show a very different trend than the yearly occurrence rates. Here, we see a slight seasonal variation of geomagnetic disturbance levels, generally weaker during austral summer and stronger during austral winter [Berthelier, 1976], with slight peaks during the equinoxes [Russell and McPherron, 1973]. However, the hiss and especially chorus occurrence rates show a very strong seasonal variation which is disproportionately greater than would be expected from the seasonal variation in geomagnetic activity alone (though there is a slight peak in hiss occurrence during the equinoxes).

[60] The large seasonal variation in chorus and hiss occurrence is the result of one of the most debilitating factors for

interpreting ground-based measurements of magnetospheric phenomena, namely variations in ionospheric absorption. Daytime absorption rates for trans-ionospheric propagation can be tens of dB higher than nighttime rates at 50° invariant latitude [Helliwell, 1965, Figure 3–35], and the signal strength is further reduced during the day due to increased absorption in the Earth-ionosphere waveguide.

[61] To illustrate the effect of ionospheric absorption on received chorus wave power, Figure 10 shows cumulative spectrograms of chorus on a monthly basis, from January to December, averaged over the full 10-year data set. The dawn day/night terminator is marked with a golden dashed line on the left of each image, and the dusk day/night terminator is marked with a blue dashed line on the right of each image. As the onset of daylight shifts to later local times from January to June, the region of observed chorus emerges between 0400 and 1000 MLT. Then as the onset of daylight moves to earlier local times from June through December, the region of observed chorus fades away. This monthly progression clearly shows that, due to increased ionospheric attenuation during daytime, chorus is only observable during local night, the times of which change dramatically throughout the year at Palmer's high geographic latitude (64.05°S). The "preferred" interval for observing chorus at Palmer is somewhere between 0400 and 1300 MLT although it is only observed between 0400 and 1000 MLT because the hours between 1000 and 1300 MLT are always sunlit.

[62] Results are similar for hiss (not shown), except that hiss is often seen at lower amplitudes below 1 kHz, even when Palmer is in daylight (as suggested by the band below 1 kHz in Figure 7 (bottom), even at local noon). This is probably the result of ionospheric absorption decreasing with decreasing frequency [e.g., Helliwell, 1965, Figure 3–35]. The hiss amplitudes below 1 kHz at dawn and dusk do however increase when Palmer is in darkness versus when it is sunlit. These results are consistent with those of *Smith et al.* [2010], who found a significantly stronger influence of the

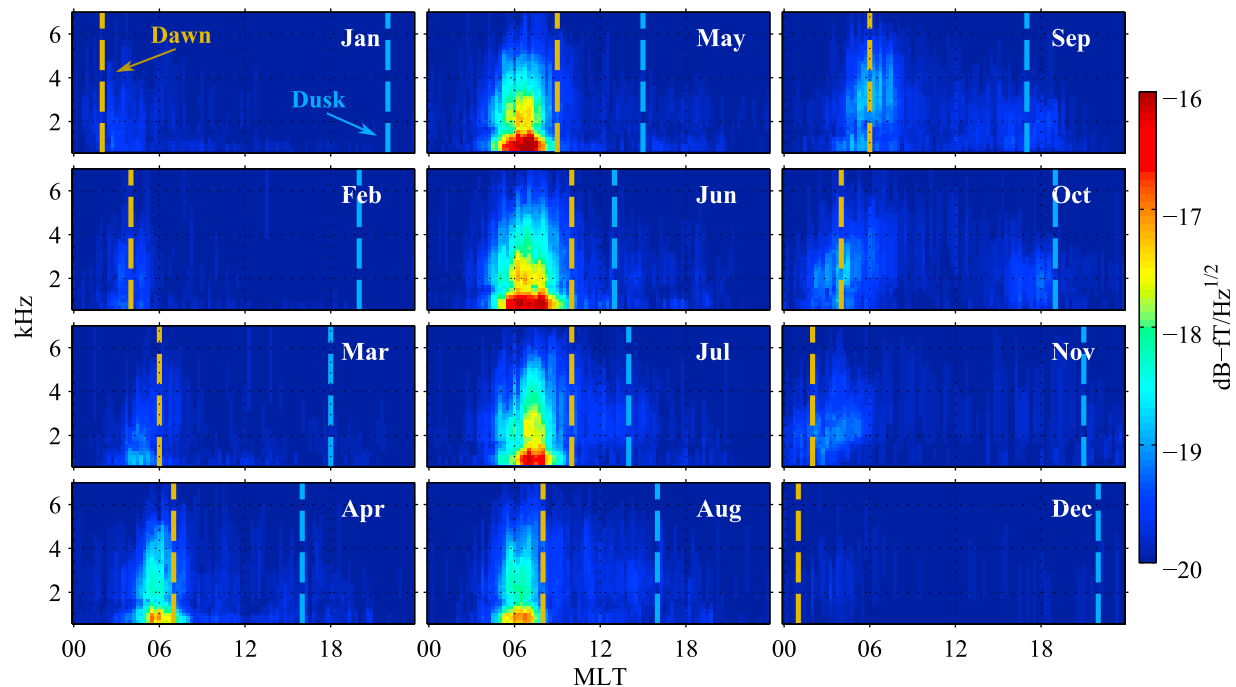


Figure 10. Cumulative spectrograms of chorus by month. The dawn terminator is shown as the golden dashed line on the left of each image, and the dusk terminator is shown as the blue dashed line on the right of each image. The region between the two terminator lines is sunlit, and the region beyond either line is in darkness. As the onset of daylight shifts to later local times from January to June, the region of chorus observations emerges between 0400 and 1000 MLT; then, as the onset of daylight moves to earlier local times from June through December, the region of chorus observations fades away. This monthly progression clearly shows that, due to increased ionospheric attenuation during daytime, chorus is only observable during local night.

day/night terminator for emissions at ~ 3 kHz than for those at ~ 1 kHz, although they did not systematically differentiate between chorus and hiss.

4. Summary and Future Work

[63] An algorithm for automatically detecting and differentiating between chorus and hiss on data from ground-based ELF/VLF wave receivers has been developed. The algorithm operates on 10-s broadband data records, sampled at 100 kHz. Data is first cleaned of sferics and hum. Next, events are detected using empirical methods and fed to a pair of previously trained neural networks which discard noise events and categorize remaining events as either chorus or hiss.

[64] All aspects of the algorithm are automatic and require no operator intervention with the exception of the initial training of the neural network. This is accomplished by having a human trainer manually create a training set by categorizing a subset of detected events as either noise, chorus, or hiss. The neural networks are then trained using this training set. The noise neural network used in this study is capable of correctly differentiating between noise and emissions for 91.9% of the 10,013 events in the noise neural network training set. The emission neural network is capable of correctly differentiating between chorus and hiss for 84.0% of the 2453 events in the emission neural training set. Excluding the one-time assembly of the neural network

training set by the trainer, the algorithm runs at 350x real time on a single modern 8-core computer and could easily run at better than real time on more conservative hardware.

[65] The algorithm was run on 10 years of broadband data from Palmer Station, Antarctica, from May 2000 through May 2010. On the basis of the output of the automated detector, we show that chorus is primarily observed in the dawn sector, at frequencies from 400 Hz to ~ 6 kHz, while hiss is observed below 1 kHz at all local times and up to ~ 4 kHz in the dusk sector. The average occurrence rates of chorus and hiss in a given year, over the course of a solar cycle, are strongly dependent on the average geomagnetic disturbance levels in that year.

[66] Over the course of a single year, chorus occurrence in particular varies significantly from June to December, as a result of the longer daylight hours and resulting increased ionospheric absorption during austral summer versus austral winter. Hiss occurrence varies in this same manner for the same reason although the difference is less dramatic due to the lower frequencies of hiss and resulting decreased ionospheric absorption. Although the perils of high ionospheric absorption in interpreting ground-based ELF/VLF wave data have long been known, Figure 10 starkly illustrates its effects and shows that caution must be used when comparing data from summer months to winter months.

[67] The scientific results presented here have only scratched the surface of the capabilities of this automated emission detector and the resulting 10-year database of

Palmer emissions. In the future, this database may be combined with similar databases of, e.g., in situ measurements of chorus and hiss, or plasmopause location, to generate statistics relating to how chorus and hiss may propagate from their source to the ground, and the attenuation suffered therein. This has been done previously via a study of how the plasmopause affects chorus propagation to the ground using a smaller data set from Palmer [Golden *et al.*, 2010]. Whistlers, which were discarded as “noise” for this study, may also be detected with some simple modifications to the neural networks. The automated detector may also be used on data from different ground stations, e.g., at different L shells, and, with some modifications, on broadband in situ satellite wave data. Thus, many different emission data sets may be easily generated from a wide variety of receivers using the same technique. Finally, as suggested earlier in section 2.6, it would be a simple matter to run the automated detector in real time at Palmer or at a similar remote site in order to produce real time measurements of chorus and hiss. We expect that this study is merely an introduction to the capabilities of the automated emission detector and the Palmer emission database, and we expect them both to continue to bear scientific fruit for some time to come.

[68] **Acknowledgments.** This work was supported by the National Science Foundation under award 0538627. Kp and AE data were obtained from the World Data Center for Geomagnetism, Kyoto. The 10.7-cm solar flux data are provided as a service by the National Research Council of Canada.

[69] Robert Lysak thanks Vikas Sonwalkar and another reviewer for their assistance in evaluating this paper.

References

- Abel, B., and R. M. Thorne (1988), Electron scattering loss in Earth's inner magnetosphere: I. Dominant physical processes, *J. Geophys. Res.*, **103**, 2385–2396, doi:10.1029/97JA02919.
- Allcock, G. M. (1957), A study of the audio-frequency radio phenomenon known as “Dawn Chorus”, *Aust. J. Phys.*, **10**, 286–298.
- Berthelier, A. (1976), Influence of the polarity of the interplanetary magnetic field on the annual and the diurnal variations of magnetic activity, *J. Geophys. Res.*, **81**, 4546–4552, doi:10.1029/JA081i025p04546.
- Bortnik, J., R. M. Thorne, and N. P. Meredith (2008), The unexpected origin of plasmaspheric hiss from discrete chorus emissions, *Nature*, **452**, 62–66, doi:10.1038/nature06741.
- Burtis, W. J., and R. A. Helliwell (1976), Magnetospheric chorus: Occurrence patterns and normalized frequency, *Planet. Space Sci.*, **24**, 1007–1010, doi:10.1016/0032-0633(76)90119-7.
- Carpenter, D. L., J. C. Foster, T. J. Rosenberg, and L. J. Lanzerotti (1975), A subauroral and mid-latitude view of substorm activity, *J. Geophys. Res.*, **80**, 4279–4286.
- Cohen, M. B., R. K. Said, and U. S. Inan (2010), Mitigation of 50–60 Hz power line interference in geophysical data, *Radio Sci.*, **45**, RS6002, doi:10.1029/2010RS004420.
- Draganov, A. B., U. S. Inan, V. S. Sonwalkar, and T. F. Bell (1992), Magnetospherically reflected whistlers as a source of plasmaspheric hiss, *Geophys. Res. Lett.*, **19**, 233–236.
- Dunckel, N., and R. A. Helliwell (1969), Whistler-mode emissions on theOGO 1 satellite, *J. Geophys. Res.*, **74**, 6371–6385, doi:10.1029/JA074i026p06371.
- Godsill, S. J., and P. J. W. Rayner (1998), *Digital Audio Restoration: A Statistical Model Based Approach*, Springer, New York.
- Golden, D. I., M. Spasojevic, and U. S. Inan (2009), Diurnal dependence of ELF/VLF hiss and its relation to chorus at $L = 2.4$, *J. Geophys. Res.*, **114**, A05212, doi:10.1029/2008JA013946.
- Golden, D. I., M. Spasojevic, F. R. Foust, N. G. Lehtinen, N. P. Meredith, and U. S. Inan (2010), The role of the plasmopause in dictating the ground-accessibility of ELF/VLF chorus, *J. Geophys. Res.*, **115**, A11211, doi:10.1029/2010JA015955.
- Green, J. L., S. Boardsen, L. Garcia, W. W. L. Taylor, S. F. Fung, and B. W. Reinisch (2005), On the origin of whistler mode radiation in the plasmasphere, *J. Geophys. Res.*, **110**, A03201, doi:10.1029/2004JA010495.
- Hayakawa, M., Y. Tanaka, T. Okada, M. Tixier, and S. S. Sazhin (1988), Substorm-associated VLF emissions with frequency drift observed in the premidnight sector, *J. Geophys. Res.*, **93**, 5685–5700.
- Helliwell, R. A. (1965), *Whistlers and Related Ionospheric Phenomena*, Stanford Univ. Press, Stanford, Calif.
- Horne, R. B., S. A. Glauert, and R. M. Thorne (2003), Resonant diffusion of radiation belt electrons by whistler-mode chorus, *Geophys. Res. Lett.*, **30**(9), 1493, doi:10.1029/2003GL016963.
- Horne, R. B., et al. (2005), Wave acceleration of electrons in the Van Allen radiation belts, *Nature*, **437**, 227–230, doi:10.1038/nature03939.
- Jørgensen, T. S. (1968), Interpretation of auroral hiss measured onOGO 2 and at Byrd Station in terms of incoherent Cerenkov radiation, *J. Geophys. Res.*, **73**, 1055–1069, doi:10.1029/JA073i003p01055.
- Laaspere, T., M. G. Morgan, and W. C. Johnson (1964), Chorus, hiss, and other audio-frequency emissions at stations of the whistlers-east network, *Proc. IEEE*, **52**(11), 1331–1349.
- Lyons, L. R., and R. M. Thorne (1973), Equilibrium structure of radiation belt electrons, *J. Geophys. Res.*, **78**, 2142–2149, doi:10.1029/JA078i013p02142.
- Lyons, L. R., R. M. Thorne, and C. F. Kennel (1972), Pitch-angle diffusion of radiation belt electrons within the plasmasphere, *J. Geophys. Res.*, **77**, 3455–3474.
- Makita, K. (1979), VLF-LF hiss emissions associated with the aurora, *Mem. Natl. Inst. Polar Res., Ser. A*, **16**, 1–126.
- Meredith, N. P., R. B. Horne, and R. R. Anderson (2001), Substorm dependence of chorus amplitudes: Implications for the acceleration of electrons to relativistic energies, *J. Geophys. Res.*, **106**, 13,165–13,178, doi:10.1029/2000JA000156.
- Meredith, N. P., R. B. Horne, D. Summers, R. M. Thorne, R. H. A. Iles, D. Heynderickx, and R. R. Anderson (2002), Evidence for acceleration of outer zone electrons to relativistic energies by whistler mode chorus, *Ann. Geophys.*, **20**, 967–979.
- Meredith, N. P., R. B. Horne, R. M. Thorne, D. Summers, and R. R. Anderson (2004), Substorm dependence of plasmaspheric hiss, *J. Geophys. Res.*, **109**, A06209, doi:10.1029/2004JA010387.
- Meredith, N. P., R. B. Horne, M. A. Clilverd, D. Horsfall, R. M. Thorne, and R. R. Anderson (2006), Origins of plasmaspheric hiss, *J. Geophys. Res.*, **111**, A09217, doi:10.1029/2006JA011707.
- Møller, M. F. (1993), A scaled conjugate gradient algorithm for fast supervised learning, *Neural Netw.*, **6**(4), 525–533, doi:10.1016/S0893-6080(05)80056-5.
- Navidi, W. (2006), *Statistics for Engineers and Scientists*, McGraw-Hill, New York.
- Nguyen, D., and B. Widrow (1990), Improving the learning speed of 2-layer neural networks by choosing initial values of the adaptive weights, in *International Joint Conference on Neural Networks 1990*, vol. 3, edited by M. Caudill, pp. 21–26, IEEE, New York, doi:10.1109/IJCNN.1990.137819.
- Parady, B. K., D. D. Eberlein, J. A. Marvin, W. W. L. Taylor, and J. L. J. Cahill (1975), Plasmaspheric hiss observations in the evening and afternoon quadrants, *J. Geophys. Res.*, **80**, 2183–2198.
- Pope, J. H. (1957), Diurnal variation in the occurrence of ‘Dawn Chorus,’ *Nature*, **180**, 433, doi:10.1038/180433a0.
- Pope, J. H. (1960), Effect of latitude on the diurnal maximum of ‘Dawn Chorus,’ *Nature*, **185**, 87–88, doi:10.1038/185087b0.
- Russell, C. T., and R. L. McPherron (1973), Semiannual variation of geomagnetic activity, *J. Geophys. Res.*, **78**, 92–108, doi:10.1029/JA078i001p00092.
- Russell, C. T., R. L. McPherron, and J. P. J. Coleman (1972), Fluctuating magnetic fields in the magnetosphere. I: ELF and VLF fluctuations, *Space Sci. Rev.*, **12**, 810–856, doi:10.1007/BF00173072.
- Said, R. K. (2009), Accurate and efficient long-range lightning geo-location using a vlf radio atmospheric waveform bank, Ph.D. thesis, Stanford Univ., Stanford, Calif.
- Santolik, O., J. Chum, M. Parrot, D. A. Gurnett, J. S. Pickett, and N. Cornilleau-Wehrin (2006), Propagation of whistler mode chorus to low altitudes: Spacecraft observations of structured ELF hiss, *J. Geophys. Res.*, **111**, A10208, doi:10.1029/2005JA011462.
- Sazhin, S. S., and M. Hayakawa (1994), Periodic and quasiperiodic VLF emissions, *J. Atmos. Terr. Phys.*, **56**, 735–753.
- Smith, A. J., M. P. Freeman, and G. D. Reeves (1996), Postmidnight VLF chorus events, a substorm signature observed at the ground near $L=4$, *J. Geophys. Res.*, **101**, 24,641–24,654, doi:10.1029/96JA02236.
- Smith, A. J., R. B. Horne, and N. P. Meredith (2004), Ground observations of chorus following geomagnetic storms, *J. Geophys. Res.*, **109**, A02205, doi:10.1029/2003JA010204.

- Smith, A. J., R. B. Horne, and N. P. Meredith (2010), The statistics of natural ELF/VLF waves derived from a long continuous set of ground-based observations at high latitude, *J. Atmos. Sol. Terr. Phys.*, **72**, 463–475, doi:10.1016/j.jastp.2009.12.018.
- Sonwalkar, V. S., and U. S. Inan (1989), Lightning as an embryonic source of VLF hiss, *J. Geophys. Res.*, **94**, 6986–6994.
- Storey, L. R. O. (1953), An investigation of whistling atmospherics, *Phil. Trans. R. Soc. London, Ser. A*, **246**, 113–141.
- Taylor, W. W. L., and D. A. Gurnett (1968), Morphology of VLF emissions observed with the Injun 3 satellite, *J. Geophys. Res.*, **73**, 5615–5626.
- Thorne, R. M., and C. F. Kennel (1967), Quasi-trapped VLF propagation in the outer magnetosphere, *J. Geophys. Res.*, **72**, 857–870.
- Thorne, R. M., E. J. Smith, R. K. Burton, and R. E. Holzer (1973), Plasmaspheric hiss, *J. Geophys. Res.*, **78**, 1581–1596, doi:10.1029/JA078i010p01581.
- Tsurutani, B. T., and E. J. Smith (1974), Postmidnight chorus: A sub-storm phenomenon, *J. Geophys. Res.*, **79**, 118–127, doi:10.1029/JA079i001p00118.
- Vershinin, E. F. (1970), About the intensity of the hiss near inner boundary of the plasmopause and about the bursts of hiss with drifting frequency, *Ann. Geophys.*, **26**, 703–707.
- Welch, P. D. (1967), The use of fast Fourier transform for the estimation of power spectra: A method based on time averaging over short, modified periodograms, *IEEE Trans. Audio Electroacoust.*, **AU-15**, 70–73.

D. I. Golden and M. Spasojevic, Electrical Engineering Department, Stanford University, 350 Serra Mall, Packard Bldg., Stanford, CA 94305-9515, USA. (dgolden1@stanford.edu)

U. S. Inan, Electrical Engineering Department, Koç University, Sariyer, 34450 Istanbul, Turkey. (inan@stanford.edu)